PIER C

A Single-Fed Broadband Circularly Polarized Antenna Based on Rotating Metasurface

Xin Qu[1], Rongxian Bai[1], Peng Wang[2], Minquan Li[1,*],
Zufeng Zhang[3], Shuang Xiao[1], Chen Li[1], and Guocui Zhu[1]

[1]*The Information Materials and Intelligent Sensing Laboratory of Anhui Province, Anhui University, Hefei 230039, China*
[2]*School of Electronic Engineering and Intelligent Manufacturing, Anqing Normal University, China*
[3]*Zufeng Zhang located in Liaoyang, China*

ABSTRACT: In this paper, a proposed design features a single-fed broadband circularly polarized antenna based on a rotating metasurface. The antenna is positioned between a rotating 4×4 periodic patch and the ground plane. The antenna comprises a driving patch and a parasitic patch. It utilizes two modes of the driving patch, which exhibit different polarizations along the two directions. When the metasurface is placed on it, the truncation angle of the metasurface cells causes the excitation of the two modes with left-rotating circular polarization (CP) and right-rotating CP, respectively. To weaken the right-handed CP relative to the left-handed CP, effectively enhancing the latter, another angle is truncated on the metasurface cell, and the metasurface is rotated by an angle. The final antenna was fabricated and tested with an overall size of $32 \times 32 \times 3 \, \text{mm}^3$. Measurements indicate that the $|S_{11}| < -10 \, \text{dB}$ bandwidth ranges from 4.72 to 7.67 GHz (47.9%), and the 3 dB axial ratio (AR) bandwidth ranges from 4.97 to 6.48 GHz (26.3%). Additionally, it achieves a peak gain of 7.75 dBi.

1. INTRODUCTION

Due to the advantages of suppressing multipath interference and reducing polarization mismatch, certain wireless communication systems necessitate antennas with broadband and CP characteristics. Wideband, compact-size, gain-flat CP antennas are also imperative to fulfill the demands of high data rate transmission and processing [1].

Researchers have developed various types of broadband circularly polarized antennas. Low-profile antennas with parasitic patches and vertical metal plates have achieved good AR bandwidth (ARBW) [2]. Broadband and efficient CP performance can be achieved using dielectric resonant antennas [3]. Moreover, designing a broadband feed network can also yield broadband AR bandwidth. In [4], a Wilkinson power divider is employed to construct a feeder network. Crossed dipoles with wide open ends and parasitic patches also significantly enhance the axial specific bandwidth, as discussed in [5].

In recent years, metasurface has been extensively researched and applied to enhance the performance of antennas. In [6], a wide AR bandwidth of 4.9–6.2 GHz (23.4%) was obtained for a single-fed CP antenna using metamaterials (MTMs). H-shaped microstrip patches printed on a metamaterial-excited electrically resistive impedance surface (RIS) structure enabled a 27.5% 3 dB AR bandwidth (4.55–6 GHz) [7]. Characteristic mode theory (CMT) has been recently applied to antenna design. Air spacing and L-slot can realize 90° difference by metasurface, and finally the proposed antenna has a 22.9% 3-dB ARBW [8]. A 5×5 array of square patches of metasurface

was analyzed by characteristic mode, and finally the proposed antenna had a 22.2% 3-dB ARBW [9].

In this paper, the proposed antenna is also implemented using a metasurface. Right CP is suppressed by the metasurface, thus achieving further enhancement of the left CP and consequently broadening the AR bandwidth. Furthermore, the developed antenna is well suited for deployment in the 5G NR (new radio) FR1 range in the Sub-6 GHz band, WLAN and Wi-Max applications [10, 11]. The experimental results from the simulations indeed demonstrate some improvement in the AR bandwidth. The advantages of this antenna, including wide S_{11}, a 3 dB AR bandwidth, stable radiation pattern, and high gain, have been validated both computationally and experimentally. The simulation work throughout this study utilizes ANSYS High Frequency Structural Simulator (HFSS).

2. ANTENNA DESIGN

2.1. Antenna Configuration

Figure 1 illustrates the antenna configuration, comprising a driving and parasitic patch situated between a clockwise-rotated $\theta = 108°$ metasurface and the ground plane, and two Rogers RO4003 substrates (with $\varepsilon_r = 3.38$ and $\tan \delta = 0.0027$). The square driver patch #1 has four truncation angles denoted as q, $q1$, $q2$, and $q3$. To further enhance the potential AR bandwidth, a parasitic patch #2 with dimensions $b1 \times b1$ is positioned adjacent to the driver patch. An expansion band of size $s \times wf$ is incorporated into the driver patch to improve S_{11}. The driver patch and parasitic patch are printed on substrate 1. Feed point is positioned off-center from
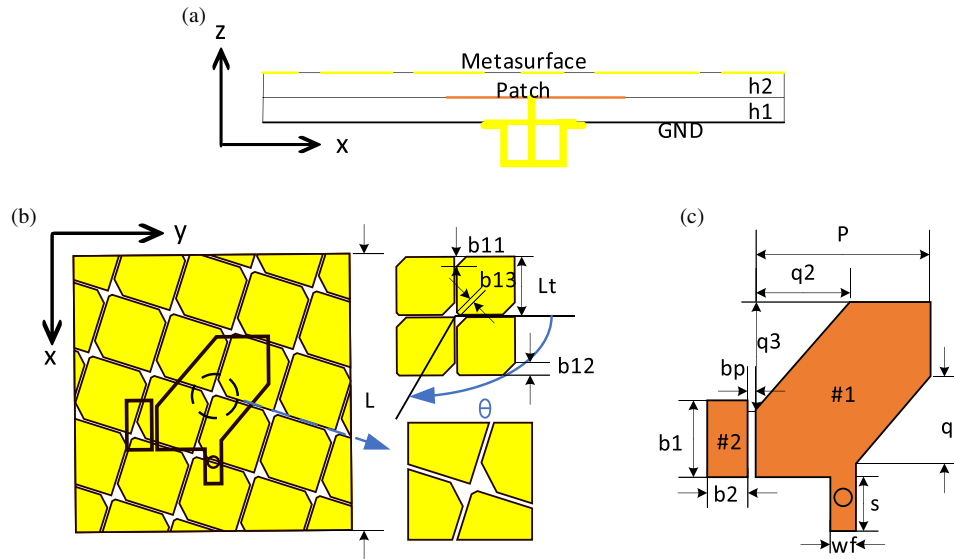
FIGURE 1. Antenna configuration. (a) Side view. (b) Top view of the first layer. (c) Top view of the second layer.
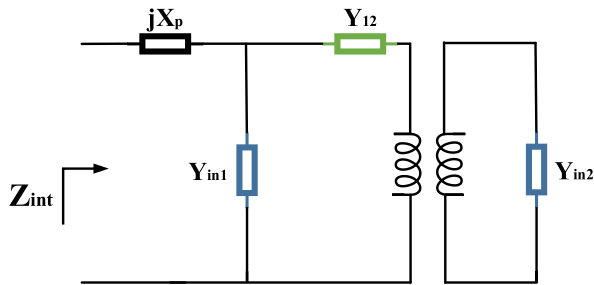

FIGURE 2. The circuit model for the entire antenna.

the patch at fx. The metasurface is printed on substrate 2, comprising 36 rectangular metal patches with truncated corners arranged in a 6×6 layout, cut into the dielectric substrate after rotation θ. The cells measure $Lt \times Lt$, with the corners cut at $b11$, $b12$, $b13$, and a gap of g between neighboring cells. To achieve a low profile of the antenna, there is no gap between the substrates. The circuit model for the entire antenna is shown in Fig. 2. The total input impedance of this antenna structure is:

$$Z_{int} = \frac{Y_{12} + N^2 Y_{in2}}{Y_{in1}(Y_{12} + N^2 Y_{in2}) + N^2 Y_{in2} Y_{12}} + jX_p \quad (1)$$

where jX_p represents the equivalent reactance introduced by the feed probe, N the voltage ratio, Y_{12} the mutual conductance between the two cavity ports, Y_{in1} the input conductance of the monolayer microstrip antenna, and Y_{in2} the input conductance of the metasurface. The center frequency is chosen as 6 GHz. The antenna is modeled in HFSS. The design optimization parameters of the antenna: $g = 0.3$ mm, $Lt = 7.2$ mm, $b11 = 1.2$ mm, $b12 = 1.5$ mm, $b13 = 0.3$ mm, $P = 13$ mm, $q = 7.5$ mm, $q1 = 1$ mm, $q2 = 7$ mm, $q3 = 8$ mm, $s = 4$ mm, $wf = 1.9$ mm, $b1 = 5.7$ mm, $b2 = 2.9$ mm, $bp = 0.6$ mm, $fx = 8$ mm, $h1 = h2 = 1.524$ mm.

2.2. Design Process of CP Antenna

The design process of the antenna is based on a truncated square microstrip antenna design as shown in Fig. 3. The dielectric substrate of this antenna is made of 3 mm thick Rogers RO4003 with a truncated square patch on the top layer and a ground layer on the bottom layer. It is analyzed by HFSS simulation to obtain S_{11} and AR, as shown in Fig. 4 below. The antenna can achieve CP performance in a narrow band. The size of the intercept angle q and the probe distance fx from the center of the coaxial feed are investigated through parameter optimization, as shown in Fig. 5. Parameter q plays a dominant role in the AR, and as q increases, the AR gradually shifts away from the center by 3 dB. The parameter fx plays a dominant role in the input impedance, and the closer the fx is to the center, the better matched the antenna is. To generate additional resonance points in the S_{11} and AR, as well as to achieve the minimum AR point, a layer of metasurface consisting of 4×4 rectangular patches is added to the modified truncated square microstrip patch antenna. The structure is illustrated in Fig. 6. The antenna is capacitively coupled to generate a resonant mode, resulting in the acquisition of two minimum AR points. Additionally,
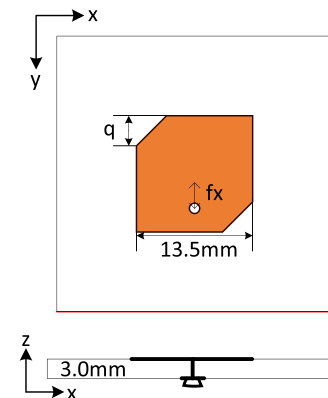

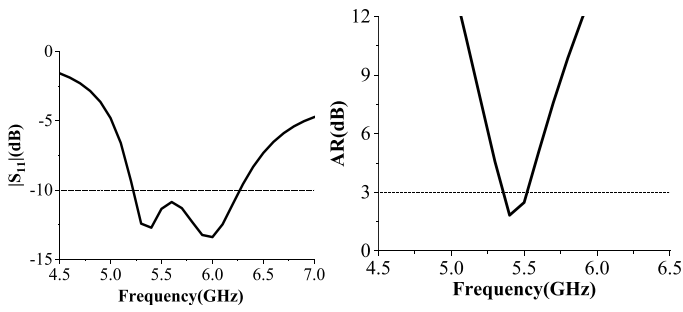**FIGURE 3**. Truncated square microstrip antenna.

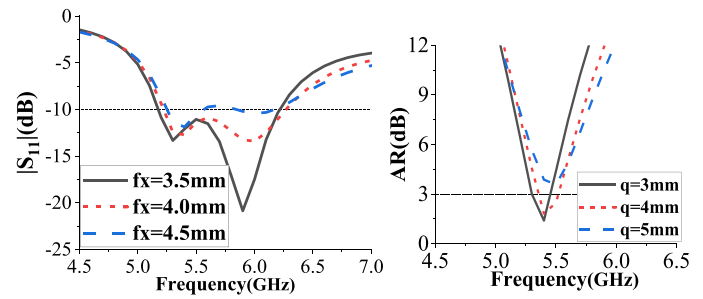**FIGURE 4.** S_{11} and AR simulations of a truncated square microstrip antenna.

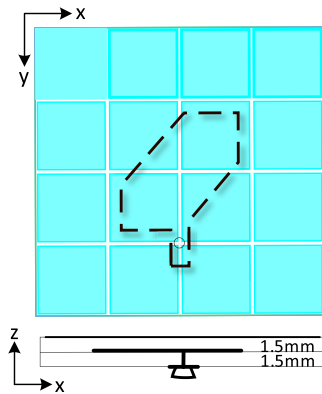**FIGURE 5.** Optimization plot for parameters fx and q.

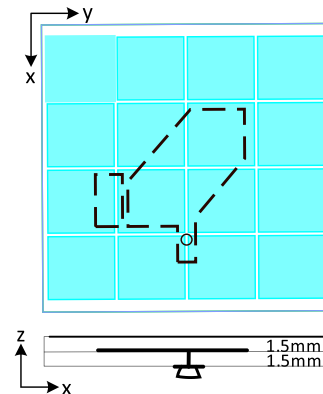**FIGURE 6.** Based on truncated square metasurface microstrip antenna 1.

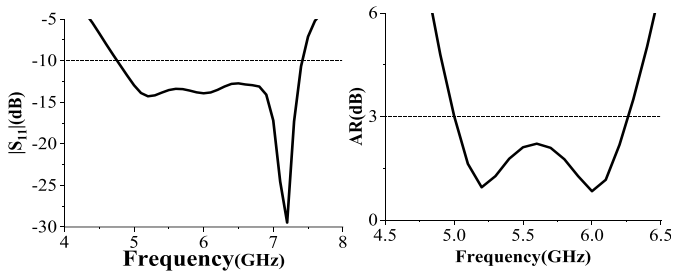**FIGURE 8.** Based on truncated square metasurface microstrip antenna 2.

FIGURE 7. S_{11} and AR simulations for the truncated square metasurface microstrip antenna 1.
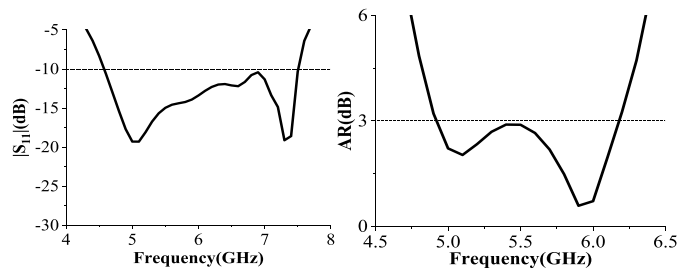

FIGURE 9. S_{11} and AR simulations for the truncated square metasurface microstrip antenna 2.

both the S_{11} and AR bandwidth are significantly increased, as shown in Fig. 7. A parasitic patch is added, in Fig. 8. The objective is to enhance the antenna's low-frequency impedance matching and shift the AR bandwidth towards lower frequencies, in Fig. 9. To increase the AR bandwidth of antenna 2, two corners are trimmed at the upper right and lower left of the antenna 2 metasurface unit. Additionally, a notch is cut in the driver patch simultaneously, in Fig. 10. The enhancement of the antenna AR is accomplished by utilizing the line polarization of the notch to generate CP on the metasurface, as demonstrated in Fig. 11. To explain the rationale behind upgrading antenna 2 to antenna 3 in order to broaden the AR, the metasurface in antenna 3 is depicted in Fig. 12(a), where a new metasurface cell can be viewed in Fig. 12(b). The notch positioned at the center of the driver patch is polarized in alignment with the electric field **E**. The electric field is resolved into two orthogonal com-

ponents, **E1** and **E2**, in Fig. 12(b). **E1** and **E2** will be viewed as two different impedances, which can be respectively written as [12]

$$Z_1 = R'_1 + jX'_1 \qquad (2)$$
$$Z_2 = R'_2 + jX'_2 \qquad (3)$$

The truncation angle widens the gap between neighboring and opposing patches, thereby increasing X'_2 and decreasing X'_1. Therefore, the amount of the cutoff angle can be used to change the phase of Z_1 and Z_2. The metasurface is designed as $|Z_1| = |Z_2|$ and $\angle Z_1 - \angle Z_2 = 90°$, and then, $|E1| = |E2|$ and $\angle E1 - \angle E2 = 90°$. **E2** leads **E1** by 90°, and the synthesized field through the metasurface is left-handedly circularly polarized and rotates clockwise as shown by the yellow arrow in Fig. 12. Therefore, the interaction between the notch and
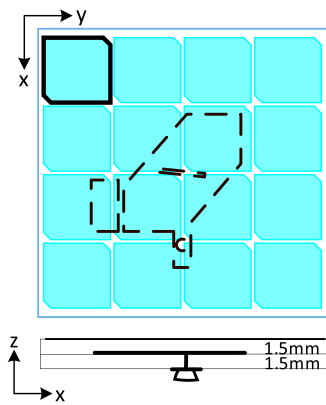
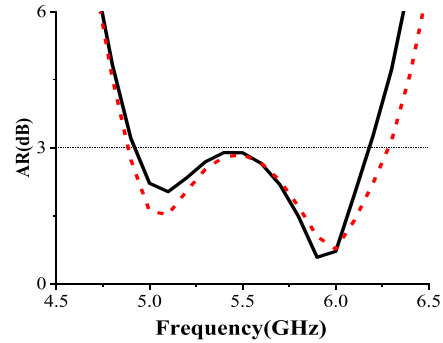**FIGURE 10.** Based on truncated square metasurface microstrip antenna 3.

FIGURE 11. The AR simulation between antenna 3 and antenna 2 based on the truncated square metasurface microstrip antenna 3.
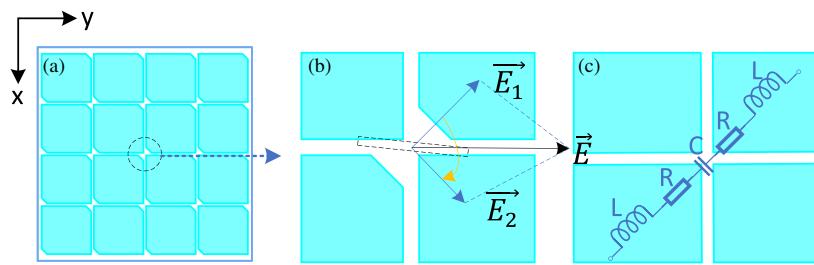

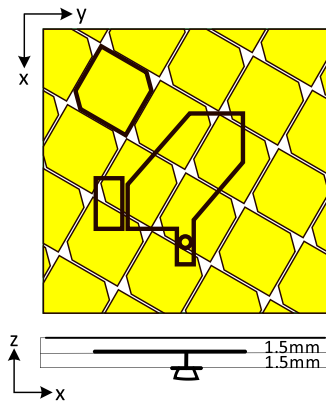**FIGURE 12.** (a) Metasurface, (b) cell with tangents, (c) cell without tangents.

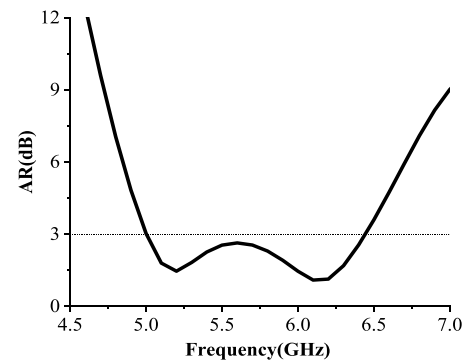**FIGURE 13.** Rotating metasurface microstrip antenna 1.

FIGURE 14. AR of rotating metasurface microstrip antenna 1.

metasurface increases the axial specific bandwidth of the antenna.

The rotating metasurface microstrip antenna 1 is based on the truncated square metasurface microstrip antenna 3. The metasurface unit is truncated on the upper left and lower right corners and rotated clockwise by an angle of 6×6. This retains the part above the dielectric substrate, while the rest is truncated, as shown in Fig. 13. The metasurface is rotated to utilize the current polarization of the patch in order to generate CP on the metasurface and enhance the antenna AR, as illustrated in Fig. 14.

In Fig. 16, the truncated square patch has two current modes, namely **E1** and **E2**, which excite the metasurface to emit left-rotating and right-rotating circularly polarized waves, as de-

picted in Fig. 15. In Fig. 16, the current has polarization along **E1** at both 0° and 90° phases. The magnitude of the polarization along **E1** is maximum at 0° phase, indicating the dominant role of the **E1** polarization. This also demonstrates that the antenna achieves left-handed CP. In order to weaken the right-handed CP compared to the left-handed CP, a corner is cut in the direction of **E22**, resulting in the rotating metasurface microstrip antenna 2. To further elucidate this mechanism, a metasurface with 3 corners cut is plotted in Fig. 15. In this figure, the pattern surrounded by black circles can be considered as new cells on the same metasurface. The driving patch produces two polarizations **E1** and **E2**. The E1 and **E2** electric fields are decomposed into two orthogonal components, **E11** and **E12**, and **E21** and **E22**, respectively. **E11** and **E12** will be considered
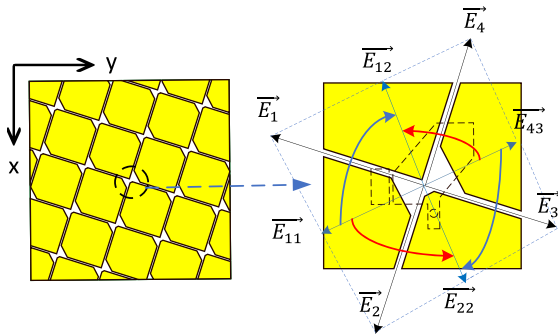
FIGURE 15. Metasurface cell with 3 tangents of rotating metasurface microstrip antenna 2.
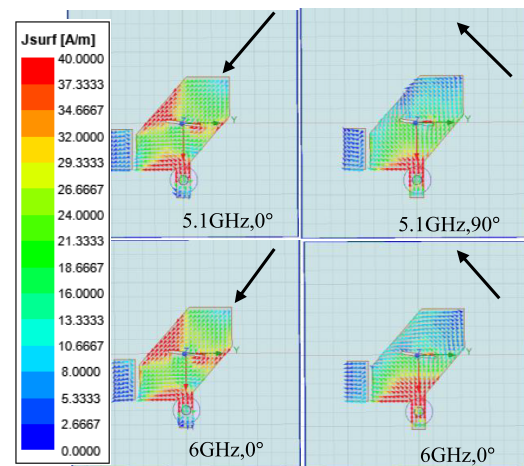

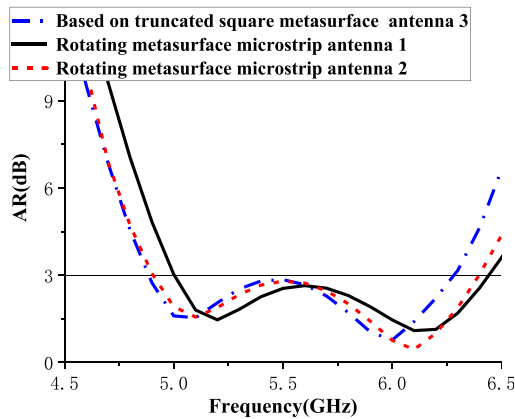**FIGURE 16**. Current distribution on driver patch and parasitic patch: 5.1 GHz and 6 GHz.

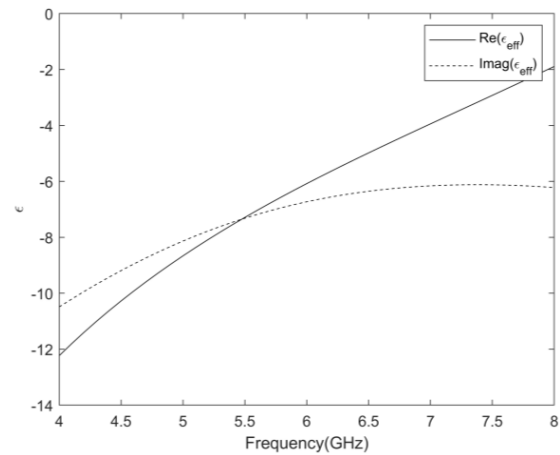**FIGURE 17**. AR of three different types of antennas.

FIGURE 18. Permittivity ϵ.

as two different impedances $Z1$ and $Z2$. The metasurface is designed such that $|Z1| = |Z2|$ and $\angle Z1 - \angle Z2 = 90°$. Subsequently, $|E11| = |E12|$ and $\angle E11 - \angle E12 = 90°$. $E11$ leads $E12$ by $90°$, resulting in the synthetic field through the metasurface being left-handed circularly polarized and rotating clockwise. Similarly, **E11** leads **E22** by $90°$, causing the synthetic field through the metasurface to be right-handed circularly polarized, rotating counterclockwise, as indicated by the blue and red arrows in Fig. 15. As a result, the interactions between the driving patch and metasurface increase the antenna's axial bandwidth. However, due to the presence of the right CP wave, the antenna matching is not very optimal. To further reduce the right CP produced by the interaction between the driving patch and the metasurface, the metasurface unit is truncated at an angle in the direction of **E22**, with the angle in the direction of **E43** slightly larger than the truncation angle in the direction of **E11**. The goal is to maintain the capacitance difference between **E11** and **E12**, and between **E43** and **E22** unchanged, meaning that the phase difference between **E11** and **E12**, as well as between **E43** and **E22**, is always kept at $90°$. Simultaneously, the capacitance difference between **E11** and **E22** is

reduced while that between **E12** and **E43** is increased, resulting in the phase difference between **E11** and **E22** being less than $90°$ and that between **E12** and **E43** being greater than $90°$. As a result, the right CP is less strongly excited than the left CP, leading to an enhanced left CP. Fig. 17 compares the AR of rotating metasurface microstrip antennas 1 and 2 with that of the truncated square-based metasurface microstrip antenna 3, demonstrating that rotating metasurface microstrip antenna 2 achieves a broader axial bandwidth. Finally, electromagnetic simulations were conducted on the metasurface cell shown in Fig. 15. The results indicate that the dielectric constant and magnetic permeability are negative between 4 and 6.5 GHz, as depicted in Figs. 18 and 19, while the refractive index is negative from 4 to 8 GHz, as illustrated in Fig. 20.

2.3. Current Analysis

To demonstrate the ability of the proposed antenna to achieve CP, the phase variation of the metasurface, specifically the current distribution at the two minimum points of the antenna's AR bandwidth (5.1 GHz and 6.1 GHz), is investigated as depicted in Fig. 21. At 5.1 GHz in the 0° phase, the current flows
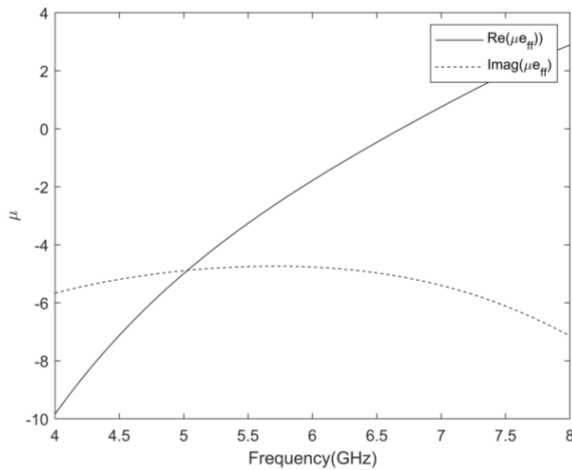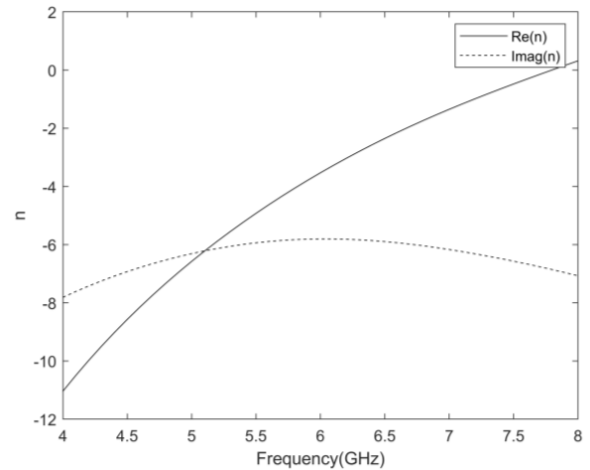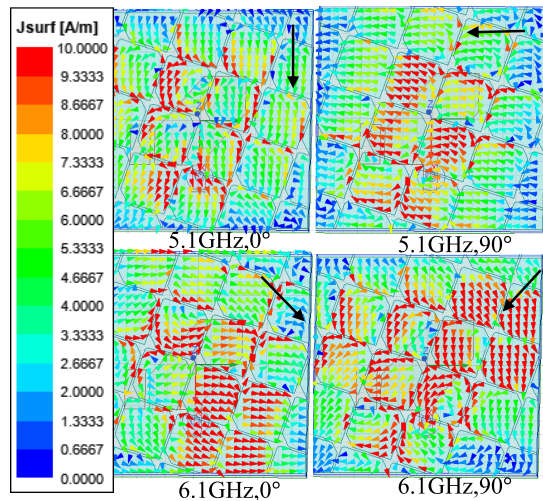
FIGURE 19. Permeability μ.

FIGURE 20. Refractive index n.

FIGURE 21. Metasurface current distribution at different phase angles: 5.1 GHz and 6.1 GHz.
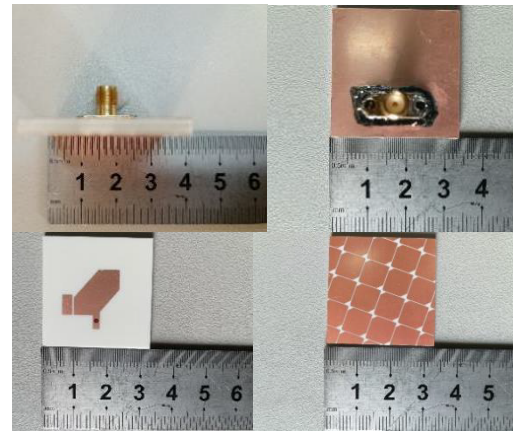

FIGURE 22. Antenna fabrication drawing.

downward, while in the 90° phase, the current flows to the left. At 6.1 GHz in the 0° phase, the predominant current flows toward the lower right direction, and in the 90° phase, it flows toward the lower left corner. The outcomes demonstrate that left circularly polarized radiation is achieved by stimulating two orthogonal modes with a 90° phase difference at 5.1 GHz and 6.1 GHz. Furthermore, at 6.1 GHz, the current distribution on the metasurface is more pronounced than that at 5.1 GHz. Specifically, at 5.1 GHz, the highest current is observed in the central metal plate of the metasurface, while at 6.1 GHz, the maximum current is distributed across all plates of the metasurface. This confirms that the dip in AR at 6.1 GHz is predominantly influenced by the metasurface, while at 5.1 GHz, it is influenced by both the driven patch and parasitic patch.

3. EXPERIMENTAL RESULTS

In order to validate the performance of the rotating metasurface antenna for circularly polarized bandwidth, a fabricated prototype sample is depicted in Fig. 22. The prototype has dimen-

sions of $32 \times 32 \times 3 \text{ mm}^3$ (approximately $0.67\lambda_0 \times 0.67\lambda_0 \times 0.06\lambda_0$ at 6.1 GHz). Fig. 23 illustrates the wide impedance bandwidth of the antenna. The measured impedance bandwidth ranges from 4.72 to 7.67 GHz (47.9%), which closely aligns with the simulated bandwidth of 4.72 to 7.56 GHz (46.3%), thus confirming the validity of the antenna design. The measured AR bandwidth is depicted in Fig. 24, ranging from 4.97 to 6.48 GHz (26.3%), in comparison to the simulated range of 4.9 to 6.4 GHz (26.5%). The difference between the measured and simulated ARs is minimal. Moreover, the gain of the antenna on one side of the metasurface was measured, and it achieved a peak gain of 7.75 dBic. The measured gain exhibits minor fluctuations relative to the simulated gain. These minor fluctuations are the result of machining errors. Furthermore, differences in the measurement process in Fig. 24, such as calibration of antennas, and circuit losses, can also contribute to the variations. For measuring the radiation patterns, a conventional broadband horn antenna is employed for signal transmission, while the constructed antenna is to capture the signal. The horn antenna remains stationary, while the constructed antenna
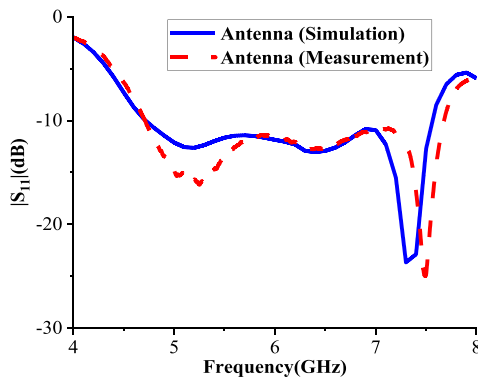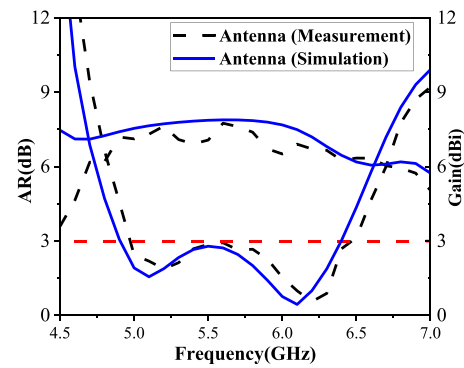
FIGURE 23. Simulated and measured S_{11}.

FIGURE 24. AR and gain for simulation and measurement.

TABLE 1. Comparing the performance of other metasurface antennas.

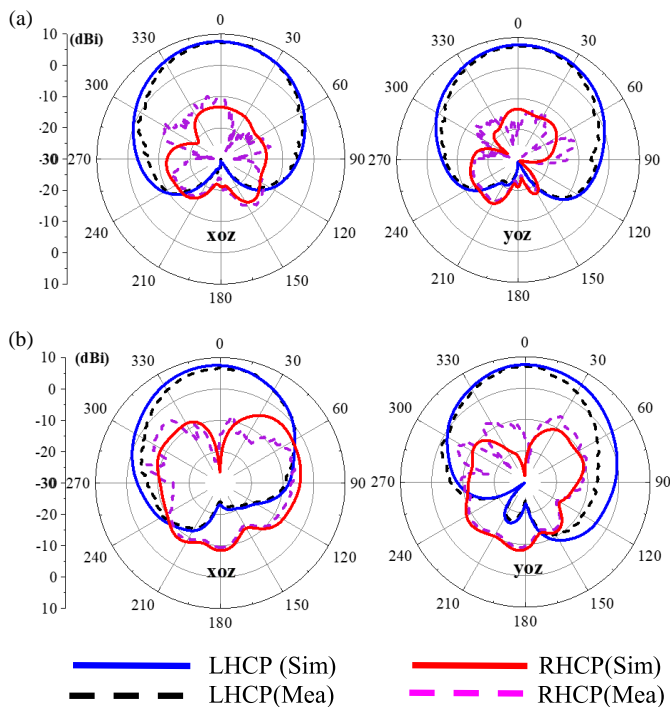| Ref.	Volume (λ_0^3 at f_0)	IBW (%)	ARBW (%)	Peak Gain (dBi)
[8]	$1.15 \times 1.15 \times 0.1$ at 6.8 GHz	37.7%	22.9%	8.7
[9]	$1.05 \times 1.05 \times 0.06$ at 6.3 GHz	43.9%	22.2%	9.3
[12]	$1.87 \times 1.86 \times 0.6$ at 7.36 GHz	6.87%	6.87%	12.31
[13]	$1.14 \times 1.14 \times 0.05$ at 4.3 GHz	18.6%	18.6%	5
[14]	$1.55 \times 1.55 \times 0.057$ at 5.8 GHz	19%	17.2%	5.66
[15]	$0.76 \times 0.76 \times 0.04$ at 4.41 GHz	33.14%	18.61%	8.96
[16]	$1.15 \times 1.15 \times 0.1$ at 6.8 GHz	37.7%	22.9%	8.7
our work	$0.67 \times 0.67 \times 0.06$ at 6.2 GHz	47.9%	26.3%	7.75

(a)

(b)

FIGURE 25. Radiation patterns for measurement and simulation at (a) 5.1 GHz, (b) 6.1 GHz.

FIGURE 26. Antenna test environment.

rotates from $-90°$ to $90°$. Fig. 25 illustrates the directional pattern patterns of the constructed antenna. The radiation exhibits a r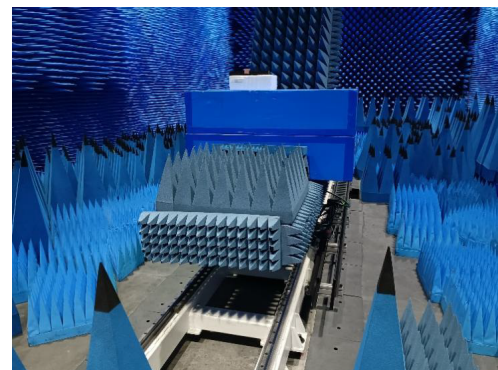ight CP. The simulation results may not align precisely with the measured ones due to the significant influence of the feeding cable and SMA connector on the measurement outcomes. These factors were not considered in the simulation model. The antenna test environment is shown in Fig. 26. Table 1 presents the performance of low-profile antennas that utilize a combination of metasurface and microstrip radiating patch as detailed in the literature [12–16]. It also provides a comparison with the proposed approach in this paper, which combines a truncated square microstrip patch with a rotating metasurface. The central frequency of the passband is designated as $\lambda_0 = C/f_0$ in terms of wavelength, where C represents the speed of light, and f_0 denotes the center frequency. The findings highlight that the designed metamaterial CP antenna exhibits a wide bandwidth, encompassing both impedance and AR bandwidths.

4. CONCLUSION

In this paper, truncated square slots are initially utilized to excite the metasurface for enhancing circular polarization properties. Subsequently, the truncated square slots are eliminated, and the truncated square patch is directly employed to improve the excitation of metasurface circular polarization. Upon observing the truncated square current mode, it is found that there are two current modes, one inducing left-handed CP and the other inducing right-handed CP after rotating the metasurface. The current distribution of the left circular polarization excitation is evidently larger, leading to the decision to weaken the excitation of right circular polarization to indirectly enhance the left circular polarization. Finally, the HFSS simulation results demonstrate an enhanced bandwidth, substantiating the correctness of the design.

ACKNOWLEDGEMENT

REFERENCES

[1] Ding, K., Y. Wu, K.-H. Wen, D.-L. Wu, and J.-F. Li, "A stacked patch antenna with broadband circular polarization and flat gains," *IEEE Access*, Vol. 9, 30 275–30 282, 2021.

[2] Li, J., H. Liu, S. Zhang, M. Luo, Y. Zhang, and S. He, "A wideband single-fed, circularly-polarized patch antenna with enhanced axial ratio bandwidth for UHF RFID reader applications," *IEEE Access*, Vol. 6, 55 883–55 892, Oct. 2018.

[3] Chowdhury, R., N. Mishra, M. M. Sani, and R. K. Chaudhary, "Analysis of a wideband circularly polarized cylindrical dielectric resonator antenna with broadside radiation coupled with simple microstrip feeding," *IEEE Access*, Vol. 5, 19 478–19 485, 2017.

[4] Hu, Y.-J., W.-P. Ding, and W.-Q. Cao, "Broadband circularly polarized microstrip antenna array using sequentially rotated technique," *IEEE Antennas and Wireless Propagation Letters*, Vol. 10, 1358–1361, Nov. 2011.

[5] Wen, L., S. Gao, Q. Luo, W. Hu, and B. Sanz-Izquierdo, "Design of a broadband circularly polarized antenna by using axial ratio contour," *IEEE Antennas and Wireless Propagation Letters*, Vol. 19, No. 12, 2487–2491, Dec. 2020.

[6] Ta, S. X. and I. Park, "Low-profile broadband circularly polarized patch antenna using metasurface," *IEEE Transactions on Antennas and Propagation*, Vol. 63, No. 12, 5929–5934, Dec. 2015.

[7] Chatterjee, J., A. Mohan, and V. Dixit, "Broadband circularly polarized H-shaped patch antenna using reactive impedance surface," *IEEE Antennas and Wireless Propagation Letters*, Vol. 17, No. 4, 625–628, 2018.

[8] Ding, Z., M. Xu, X. Li, S. Tao, H. Wang, and Y. Wang, "Design of wideband circularly polarized metasurface antenna using characteristic mode analysis," *Microwave and Optical Technology Letters*, Vol. 65, No. 6, 1794–1799, 2023.

[9] Liu, S., L. Yang, Q. Chen, and X. Wu, "A low-profile broadband circularly polarized metasurface antenna aperture coupled by shorted annular-ring slot," *International Journal of Antennas and Propagation*, Vol. 2022, No. 1, 8517646, 2022.

[10] Aziz, R. S. and S. Koziel, "Circularly polarized metalens antenna design for 5G NR sub-6 GHz communication systems," *AEU — International Journal of Electronics and Communications*, Vol. 173, 155024, 2024.

[11] Guthi, S. and V. Damera, "High gain and broadband circularly polarized antenna using metasurface and CPW fed L-shaped aperture," *AEU — International Journal of Electronics and Communications*, Vol. 146, 154109, 2022.

[12] Zhu, H. L., S. W. Cheung, X. H. Liu, and T. I. Yuk, "Design of polarization reconfigurable antenna using metasurface," *IEEE Transactions on Antennas and Propagation*, Vol. 62, No. 6, 2891–2898, Jun. 2014.

[13] Rajanna, P. K. T., K. Rudramuni, and K. Kandasamy, "A high-gain circularly polarized antenna using zero-index metamaterial," *IEEE Antennas and Wireless Propagation Letters*, Vol. 18, No. 6, 1129–1133, 2019.

[14] Liu, L., H. Chen, H. Sun, Z. Jin, L. F. Chernogor, D. O. Batrakov, T. Liu, and Z. Sun, "A broadband circularly polarized antenna based on transparent conformal metasurface," *IEEE Antennas and Wireless Propagation Letters*, Vol. 22, No. 12, 3197–3201, Dec. 2023.

[15] Zheng, Q., C. Guo, J. Ding, and G. A. E. Vandenbosch, "A broadband low-RCS metasurface for CP patch antennas," *IEEE Transactions on Antennas and Propagation*, Vol. 69, No. 6, 3529–3534, Jun. 2021.

[16] Kedze, K. E., H. Wang, Y. B. Park, and I. Park, "Substrate dielectric constant effects on the performances of a metasurface-based circularly polarized microstrip patch antenna," *International Journal of Antennas and Propagation*, Vol. 2022, No. 1, 3026677, 2022.